Ocean-Ionosphere Disturbances Due To the 15 January 2022 Hunga-Tonga Hunga-Ha'apai Eruption

M. Ravanelli, E. Astafyeva, Edhah Munaibari, Lucie Rolland, D.T. Mikesell

Geophysical Research Letters

RESEARCH LETTER
10.1029/2022GL101465

Ocean-Ionosphere Disturbances Due To the 15 January 2022 Hunga-Tonga Hunga-Ha'apai Eruption

M. Ravanelli[1], E. Astafyeva[1], E. Munaibari[2], L. Rolland[2], and T. D. Mikesell[3]

[1]Université Paris Cité, Institut de physique du globe de Paris (IPGP), Paris, France, [2]Université Côte d'Azur, Observatoire de la Côte d'Azur, CNRS, IRD, Géoazur, Valbonne, France, [3]Norwegian Geotechnical Institute, Natural Hazards, Oslo, Norway

Key Points:

- Joint study of oceanic and ionospheric response in New Caledonia-New Zealand and Chile-Argentina to the 15 January 2022 volcanic eruption
- Near-surface propagating Lamb wave caused a small tsunami in the ocean (air-sea wave) and unusually strong disturbances in the ionosphere
- Inversely, the eruption-generated tsunami showed significant wave heights in the ocean and much smaller response in the ionosphere

Supporting Information:

Supporting Information may be found in the online version of this article.

Correspondence to:

M. Ravanelli,
ravanelli@ipgp.fr

Citation:

Ravanelli, M., Astafyeva, E., Munaibari, E., Rolland, L., & Mikesell, T. D. (2023). Ocean-ionosphere disturbances due to the 15 January 2022 Hunga-Tonga Hunga-Ha'apai eruption. *Geophysical Research Letters*, *50*, e2022GL101465. https://doi.org/10.1029/2022GL101465

Received 1 OCT 2022
Accepted 18 MAR 2023

Abstract We investigate the oceanic and ionospheric response in New Caledonia-New Zealand and Chile-Argentina to the 15 January 2022 Hunga-Tonga volcanic eruption. For the first time, we highlight a reversed response in the oceans and in the ionosphere in terms of the amplitudes. The sea-surface fluctuations due to the passage of the atmospheric Lamb wave (i.e., air-sea wave) were not remarkable while the related ionospheric perturbation was considerable. Reversely, the eruption-induced tsunami ("regular" tsunami) caused major variations in sea-surface heights (~1 m near the volcano and ~2 m along the Chilean coastline), whereas the associated ionospheric perturbation was quite small. The observed large-amplitude ionospheric response due to Lamb waves propagation is difficult to explain, and the coupling between the Lamb wave and the ionosphere is not well-understood yet. For the first time, we estimate the delay between the Lamb waves and their signatures in the ionosphere to be ~12–20 min.

Plain Language Summary The eruption of Hunga-Tonga volcano produced a variety of atmospheric and tsunami waves recorded all over the world. We study the impacts of the eruption together on the oceans and in the ionosphere in New Caledonia-New Zealand (near the volcano) and Chile-Argentina (far from the volcano). At the sea surface, we observe two phenomena causing sea-height variations. The first is a small tsunami (air-sea wave) created by the Lamb wave: the high-pressure atmospheric wave triggered by the eruption. The second is the tsunami induced by the eruption itself. Spectacularly, at 300 km altitude, in the ionosphere, we observe perturbations in the electron content caused by the Lamb wave and by the regular tsunami. We are the first to report on the reversed amplitude of the two phenomena in the oceans and in the ionosphere. The sea-surface perturbation caused by the Lamb wave was not significant, while ionospheric perturbation was considerable. In contrast, the regular tsunami wave produced major variations. For the first time, we estimate the time delay between the Lamb wave and its signature in the ionosphere.

1. Introduction

On 15 January 2022 the Hunga Tonga-Hunga Ha'apai (HTHH) volcano violently erupted and emitted a plume to an altitude of more than 50 km (X. Liu et al., 2022; Wright et al., 2022): at least five major explosions occurred between ~04:08 and 08:20 UT (Astafyeva et al., 2022).

Volcanic eruptions can produce gravity, acoustic-gravity, and acoustic waves that can perturb the ionosphere, generating the so-called co-volcanic ionospheric disturbances (CVIDs) (Aa et al., 2022; Astafyeva, 2019; Dautermann et al., 2009; Heki, 2006; Manta et al., 2021; Meng et al., 2019; Shestakov et al., 2021; Shults et al., 2016). The HTHH eruption generated a variety of atmospheric waves detected all over the world (Matoza et al., 2022; Themens et al., 2022). Among these waves, the generation of Lamb waves that traveled four times around the Earth over the following 6 days (Matoza et al., 2022), is the most enigmatic phenomenon.

Lamb waves are non-dispersive atmospheric pressure waves (Kubota et al., 2022) that can propagate in the lower atmosphere (Nishida et al., 2014). Their typical velocity is about 315 m/s, that is, close to the speed of sound, and, depending on the local atmospheric conditions, it may vary between 300 and 360 m/s. The characteristic frequencies of the Lamb waves range between ~0.2 and 10 mHz (Nishida et al., 2014). Previously, Lamb waves were detected following the 1883 Krakatoa and Mt Saint Helen eruptions (Abercromby et al., 1888; C. H. Liu et al., 1982; Symons et al., 1888; Watada & Kanamori, 2010).

Besides the disturbances in the ionosphere, the propagation of the Lamb waves over the oceans caused perturbations in the sea level. This phenomenon is known as an air-wave-driven-tsunami or an air-sea wave (Kubota

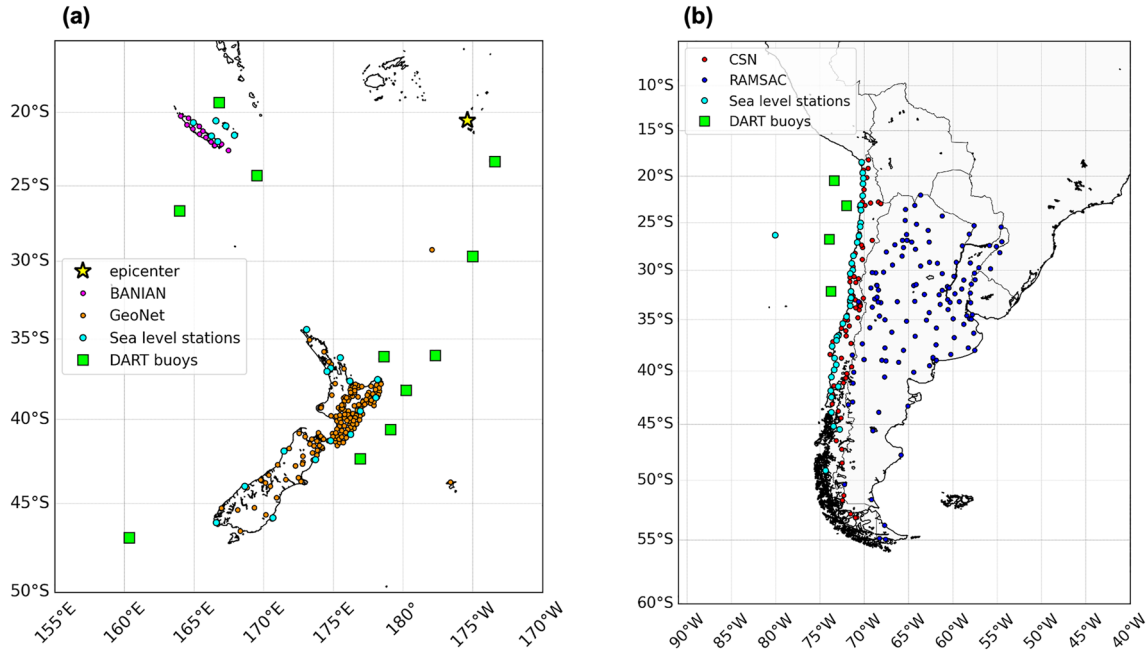

Figure 1. (a) Near field data sets: New Caledonia Global Navigation Satellite System (GNSS) (BANIAN, magenta) and New Zealand GNSS (GeoNet, orange). (b) Far field data sets: Chile GNSS (CSN, red) and Argentina GNSS (RAMSAC, blue). In both panels, sea level stations (IOC-Unesco) and DART buoys (NOAA) are depicted in cyan and green, respectively.

et al., 2022; Lynett et al., 2022; Omira et al., 2022). It was first hypothesized by Proudman (1929) after the Krakatoa event. An atmospheric pressure wave propagates along the ocean surface and pushes dynamically the water surface, causing a tsunami of atmospheric origin similar to a meteo-tsunami (Vilibić et al., 2016). The HHTH Lamb wave-related tsunami was recorded all around the Pacific (e.g., Japan, California) and in the Caribbean (Carvajal et al., 2022; International Tsunami Information Center, 2022; Kubota et al., 2022; Kulichkov et al., 2022; Nishikawa et al., 2022; NOAA, 2022b).

Here, we present the first detailed joint analysis of the link between the oceanic and ionospheric disturbances in New Caledonia-New Zealand (the near field, ~3,500 km west/southwest from the volcano) and in Chile-Argentina (the far field, ~9,000–10,000 km southeast from the volcano). We highlight for the first-time a reversed response in terms of amplitudes, and we estimate the time delay between the Lamb waves and their signature in the ionosphere. This is the first comprehensive study about the Tonga ionospheric response in South America.

2. Observational Data Set and Methodology

Global Navigation Satellite System (GNSS) technology is routinely used to sound the ionosphere by estimating the ionospheric total electron content (TEC), which represents the overall electron content along the line-of-sight path between a satellite and a receiver. Here we processed data from four ground-based GNSS networks (Figure 1): 15 stations from New Caledonia network BANIAN (Direction des Infrastructures, de la Topographie et des Transports terrestres (DIIT), 2022), 176 stations from the New Zealand GeoNet (Earthquake Commission and GNS Science, 2022), 91 stations from the Chilean CSN (Centro Sismológico Nacional, Universidad de Chile, 2022), and 122 stations from the Argentina RAMSAC (Instituto Geográfico Nacional de la República Argentina, 2022; Piñón et al., 2018). The observation rate of the BANIAN is 10 s, and that of the RAMSAC is 15 s. Both the Chilean and New Zealand networks provide 1-s data.

To retrieve GNSS-TEC variations, we apply the VARION algorithm (Ravanelli et al., 2020, 2021; Savastano et al., 2017). VARION is based on the single time differences of geometry-free combination and only relies on a standalone GNSS receiver and standard GNSS broadcast products.

In this study, we employ vertical TEC (VTEC) variations in order to normalize the TEC amplitude and to avoid effects of low elevation angles (e.g., Astafyeva, 2019). The elevation angle cutoff is taken at 30°. Furthermore, long-period variations are filtered out using a Butterworth-bandpass filter with 5–25 min period.

VTEC estimates are spatially and temporally referenced to the so-called Ionospheric Pierce Points (IPPs) representing the intersection of the satellite-receiver line-of-sight with a thin ionosphere layer at a defined altitude used to approximate the whole ionosphere. Commonly, the ionospheric layer is placed at the height of the maximum electron density. In this study, we use the altitude of 300 km for New Caledonia-New Zealand and 250 km for Chile-Argentina; these are derived from the nearest ionosonde stations situated at NIUE (19.07°S, 169.93°W) (Digital Ionogram DataBase, 2022a) and at SANTA MARIA (29.728°S, 53.714°W) (Digital Ionogram DataBase, 2022b), respectively. Furthermore, we use the eruption time calculated by the US Geological Survey (USGS, 2022).

To study the water surface response to the HTHH eruption, we use DART observations (NOAA, 2022a) and sea-level measurements (Intergovernmental Oceanographic Commission of UNESCO, 2022). We use 15-s data from 11 DART sites placed near the coastlines of New Caledonia and New Zealand and 15-min measurements from 4 DART buoys along the coastline of Chile (green squares in Figures 1a and 1b, respectively). We use 1-min sea-level measurements from 22 sites in New Caledonia-New Zealand and 38 sites in Chile (cyan dots in Figures 1a and 1b, respectively).

3. Results and Discussions

3.1. Response in New Caledonia-New Zealand

Movie S1 shows the dynamics of the sea and ionospheric disturbances between 04:00 and 12:00 UT. The Lamb waves arrive at ∼05:35 UT in New Caledonia and at ∼05:55 UT in New Zealand. Unfiltered sea level and DART measurements can be found in Figures S1a, S1b, and S2 in Supporting Information S1, respectively.

The eruption-driven tsunami (or "regular tsunami") starts at ∼06:36 UT. The maximum tsunami wave heights of 1.13 m were reached at Ouinne, New Caledonia and 0.91 m at Jackson Bay, New Zealand (International Tsunami Information Center, 2022).

Figures 2a and 2b respectively present sea-level measurements and DART data detrended with a 10th order polynomial (following Matoza et al., 2022) and sorted according to the site distance from the eruption location.

DART measurements show clearly Lamb waveforms (from ∼06:00 UTC) followed by the regular tsunami (starting from ∼07:00 UT). We note that, in DART data, Lamb wave has a distinctly different waveform and has bigger amplitude than in the sea-level measurements (only seen at Ouinne and Lifou stations). Such a difference can be explained by the fact that DART buoys, unlike tide gauges, are equipped with a seafloor bottom pressure recorder able to detect water pressure changes. The regular tsunami signature is clearly identifiable in both DART and sea-level data.

Figure 2c depicts hodochron for ionospheric TEC measurements in New Caledonia-New Zealand. A hodochron (travel-time diagram) displays TEC temporal variations versus distance from the epicenter. From hodochrons, by interpolating the maxima/minima TEC values, we can estimate the CVID velocity and interpret their nature.

In Figure 2c, we identify three distinguished ionospheric disturbances/patterns. CVID#1 has a propagation speed of ∼690 m/s and amplitudes peaking around 0.3 TECU. It is first detected at ∼05:20 UT, and based on its velocity and the arrival time, we consider this CVID to be driven by acoustic waves propagating directly from the volcano. Normally, natural hazard-driven acoustic waves cannot propagate farther than ∼600–1000 km from the source (e.g., Astafyeva, 2019; Shults et al., 2016). However, strong events, such as massive atmospheric explosions, generate acoustic pulses with large amplitudes that are detectable at larger distances. In addition, the propagation of strong acoustic waves is often non-linear, and present a broader spectrum of frequencies. In the case of the HTHH eruption, the amplitude of the near-field acoustic waves was enormous (Astafyeva et al., 2022). Therefore, it is likely that the pulse generated by the explosion reached as far as New Caledonia-New Zealand.

CVID#2 was detected between ∼06:10 and ∼07:10 UT, and is characterized by a velocity of ∼353 m/s and the maximum amplitude of 1.1 TECU, the largest amplitude of the three CVIDs. Based on this velocity and on TEC waveforms (Figure 2d), we attribute this CVID to the Lamb wave. A spectrogram for the LOS WPUK-G10 TEC data (Figure S3 in Supporting Information S1) displays a frequency peak at 1.2 mHz, the typical Lamb wave frequency (Nishida et al., 2014).

CVID#3 represents ionospheric disturbances with amplitudes up to 0.25 TECU (Figure 2d) and a velocity of ∼290 m/s. Based on their velocities and the arrival times, we attribute these CVIDs to the passage of the regular

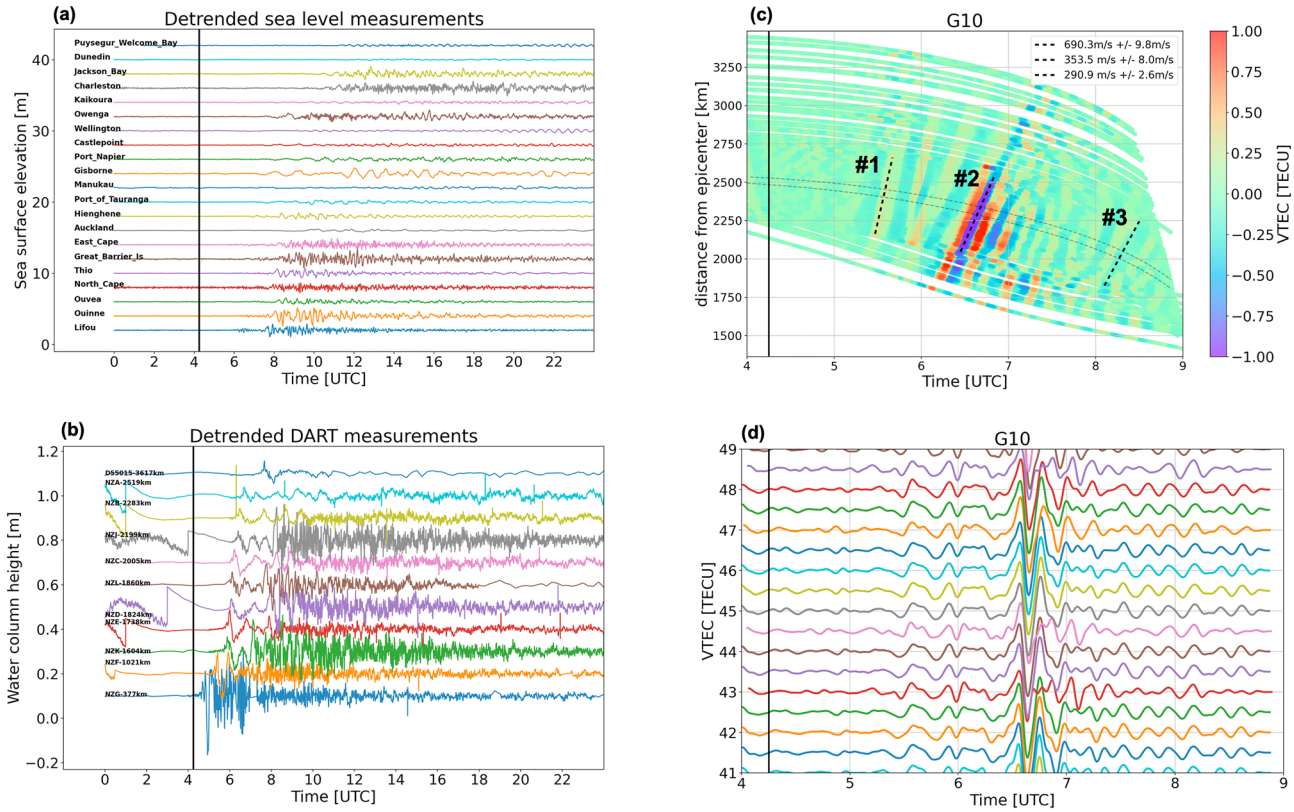

Figure 2. (a) Detrended sea level measurements along the New Caledonia-New Zealand coasts. All the stations illustrate the passage of the regular tsunami waves starting around 07:00 UT. (b) Detrended DART observations reveal the passage of the Lamb wave and the regular tsunami. (c) G10 hodochron in which the three significant co-volcanic ionospheric disturbances are highlighted. The gray dotted lines represent the SIP tracks of the borderline total electron content time series that are depicted in panel (d), in which the signatures of the acoustic waves, Lamb waves, and the tsunami can be observed.

tsunami waves. This pattern could also represent the Pekeris mode, which is a global internal atmospheric resonance mode observed after the HTHH eruption and propagating at 245 m/s (Watanabe et al., 2022). However, further studies are necessary to confirm the possibility of the coupling between the Pekeris mode and the ionosphere. It is also possible that the regular tsunami CVID was reinforced by secondary gravity waves generated by the Lamb wave propagation, giving rise to a superposition of effects as also highlighted by Santellanes et al. (2022). A similar succession of CVIDs is retrieved using other satellites (e.g., G32 in Figure S4 in Supporting Information S1).

We note that the TEC variations, except for the acoustic mode, show similar spatio-temporal patterns to the atmosphere/sea variations observed by DART and sea-level measurements (Movie S1). Figure S5a in Supporting Information S1 shows Lamb wave-related ionospheric disturbance that are perfectly aligned with the radial Lamb wavefront. Figure S5b in Supporting Information S1 depicts the tsunami wavefront and the related tsunami induced ionospheric disturbance at 08:16 UT.

However, Movie S1 shows that TEC signatures occur some time after the Lamb wave passage. Because the coupling between the Lamb waves and the ionosphere is not well understood yet, the propagation time of the Lamb waves up to the ionospheric heights is not known. To shed the light on this fundamental question, for the first time, we estimate the time delay between the two, using unfiltered data to avoid artifacts and time shifts in the arrival time estimations. Since the TEC variations include both temporal and spatial variations along the IPP/SIP track, we fix the geometry of observation by choosing a point called observation point (rhombus in Figure 3b). t_{TEC_0} is the time of the theoretical passage of the Lamb wave at the observation point, assuming an horizontal velocity of 315 m/s and the origin time of 04:15 UT. At time t_{TEC_1}, we observe the arrival of the CVID. The delay between t_{TEC_1} and t_{TEC_0} is ~15 min (bottom panel of Figure 3a). For other DART stations and TEC variations, we obtain the delay ranging between 12 and 20 min. Using a waveform correlation method and

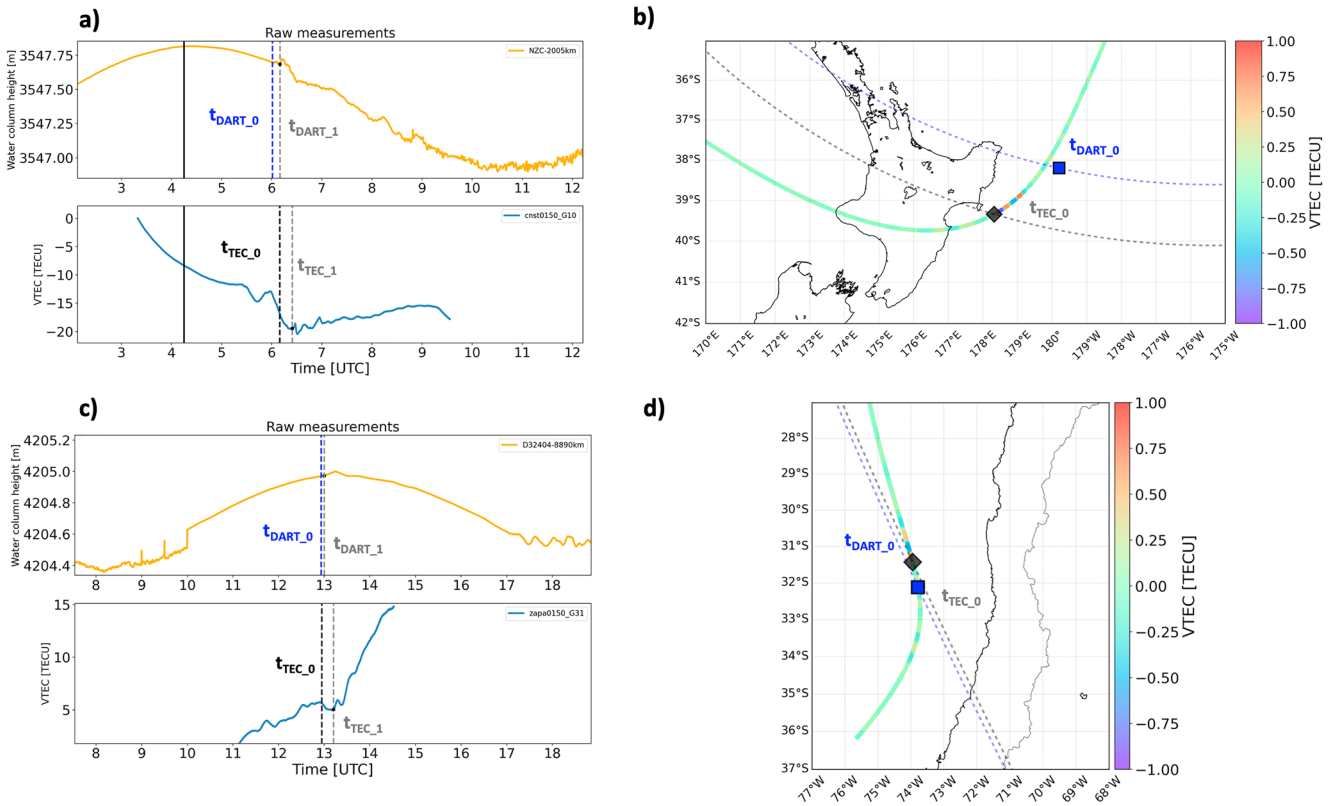

Figure 3. (a–c) Upper panels. The orange time series show the raw NZC and D32404 DART measurements, placed respectively near New Zealand and Chilean coasts. The black line represents the USGS onset time, the blue dashed line depicts the theoretical arrival time of the Lamb wave at the DART sites (t_{DART_0}), assuming the velocity of 315 m/s. The black point and the gray dashed line represent the arrival time of the Lamb wave at the DART sites (t_{DART_1}). (a–c) Bottom panels. The blue time series represent the unfiltered vertical total electron content (VTEC) measurements from CNST-G10 (New Zealand) and ZAPA-G31 (Chile), respectively. The dashed line depicts the theoretical arrival time of the Lamb wave at our observation point (t_{TEC_0}). The black dot and the gray dashed line represent the starting of the perturbation in our observation point (t_{TEC_1}). (b–d): The DART buoy location is shown by blue rectangle, the total electron content (TEC) observation point—by gray rhombus. The theoretical arrival time of the Lamb wave at DART (t_{DART_0}) is depicted as dashed blue line, at the TEC observation point (t_{TEC_0})—by dashed black line. The maps also represent filtered VTEC time series to better enhance the related Lamb wave co-volcanic ionospheric disturbance.

different assumptions, Munaibari et al. (2023) show a very small delay (1 to 5 seconds) between the Lamb wave in the DART data and its signature in the GNSS-TEC data South of New Zealand.

This delay is between the nominal propagation times of the acoustic (7–10) and gravity (15–60 min) waves. Indeed, Lamb waves bridge the gap between acoustic and acoustic-gravity modes since they can occur over a range of periods between several minutes to less than 1 day (Vergoz et al., 2022). However, unlike the acoustic and gravity waves, Lamb waves are surface-guided, that is, they are trapped in the troposphere at the boundary with the ocean or solid Earth. Because their energy remains trapped in the troposphere, their amplitude decays exponentially with altitude (Nishida et al., 2014; Santellanes et al., 2022). Energetic events like the Tonga eruption can cause Lamb wave energy tunneling from the troposphere to the thermosphere and induce stronger, and even non-linear, coupling at thermospheric heights and cause greater ionospheric disturbance. In HTHH case, the energy release was unprecedented (Astafyeva et al., 2022; Matoza et al., 2022).

In Figures 3a and 3b we also notice a delay between the theoretical arrival time of the Lamb wave and its signature in DART. We estimate the theoretical arrival time (t_{DART_0}) of the Lamb wave at the DART location and we manually pick the arrival time (t_{DART_1}) of the Lamb wave in the DART data. We find that the delay between the theoretical and the arrival times around 6–11 min. The delay could be due to a weaker air-sea coupling in shallow water as reported by Yamada et al. (2022).

The delay could also be explained by a later onset time than that estimated by the USGS. To investigate this, we employ ordinary least squares (starting from our arrival times) to make an inversion and to estimate the actual onset time and the velocity of propagation, simulating a circular wave approximation for the Lamb wave

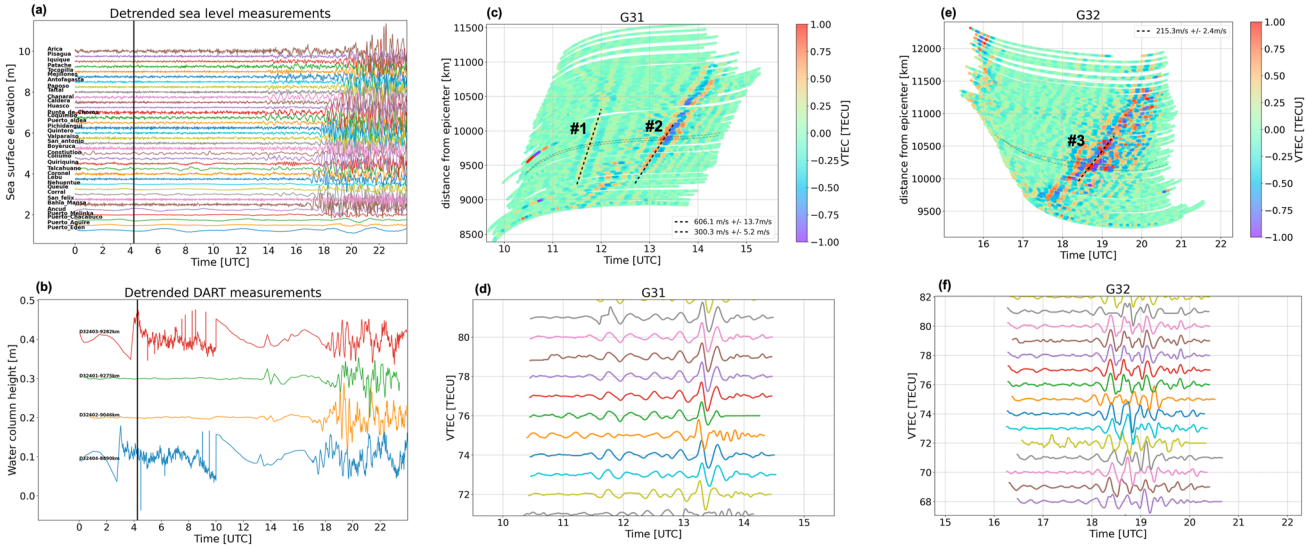

Figure 4. (a) Detrended sea level measurements along the Chilean coast. One can see the passage of the Lamb wave at ∼13:30 UT, and the regular tsunami waves starting around 18:00 UT. (b) All the detrended DART observations reveal the passage of the Lamb wave around 13:40 UT, and the regular tsunami around 17:40 UT. (c, e) G31 and G32 hodochrons are respectively showing the CVID#1, CVID#2, and CVID#3 pattern in total electron content (TEC) data. The gray dots represent the SIP tracks of the borderline TEC time series depicted in panels (d and f), respectively.

propagation (Text S1 in Supporting Information S1). We find the onset time of 04:26 UT and a velocity of 322 m/s. This strengthens the idea that the main explosion and Lamb wave emission occurred between 04:20 and 04:30 UT as already outlined by Astafyeva et al. (2022) and Vergoz et al. (2022).

3.2. Response in Chile-Argentina

The sea and ionospheric disturbances above Chile and Argentina during the first passage of the Lamb wave and during the tsunami arrivals, that is, between 12:00 and 23:30 UT, can be analyzed from Movie S2 and Figures 3c, 3d, and 4. Raw sea-level data and DART measurements can be found in Figures S6a, S6b, and S7 in Supporting Information S1.

Sea-level measurements along the Chilean coast, and especially at the Coliumo, Coquimbo, Puerto Aldea, Chanaral, and Arica sites, show small-amplitude variations related to the passage of the Lamb wave (Figure 4a). The variations are seen from 12:40 UT, which is coherent with the ∼300 m/s Lamb wave generated by the eruption. We note that this observation is different from observations in New Zealand-New Caledonia, where we hardly see Lamb waves in the sea-level measurements.

We remark that the Lamb wave is better visible in four DART measurements along the Chilean coast (Figure 4b) like for the near-field case.

Furthermore, both the sea-level and DART recorded the regular tsunami waves all along the Chilean coast. Figures 4a and 4b clearly show the regular tsunami arrival starting from 18:00 UT and having a slower moveout than the air-sea wave. The maximum regular tsunami wave height of 1.74 m was reached in Chanaral (International Tsunami Information Center, 2022).

At ionospheric heights, and similar to the near-field response westward of the volcano, three clear CVID signatures are observed above Chile and Argentina. We attribute CVID#2, the largest pattern, to the Lamb wave (Figures 4c and 4d). CVID#2 occurs between 12:30 and 14:30 UT, ∼8.2–10.2 hr after the main explosion. Its apparent horizontal velocity is ∼303 m/s (Figure 4c), and its arrival times are consistent with a travel time of 8.5 hr to the distance of 9,500 km. Spectral analysis (Figure S8 in Supporting Information S1) shows spectral power peaks around 1 mHz, which is in the frequency range of the Lamb waves (Matoza et al., 2022; Nishida et al., 2014). TEC waveforms (Figure 4d) are similar to the Lamb waveforms retrieved at nearby infrasound stations and atmospheric pressure stations (Amores et al., 2022; Vergoz et al., 2022). Finally, the CVID aligns

spatially with the Lamb wavefront over South America (Figure S5c in Supporting Information S1). This feature is even more evident in Movie S2 from 12:24 UT.

CVID#1 occurs between 11:30 and 12:00 UT, 1 hr before the Lamb waves arrival. It has lower TEC amplitude and an apparent horizontal velocity of 606 m/s (Figure 4c). Based on this velocity value, the disturbance should be linked to the propagation of acoustic wave. However, it is an unusual observation because, as mentioned previously, normally the acoustic waves cannot propagate to such long distances. Besides, if the waves were caused by the eruption and propagated from the volcano at constant speed 606 m/s, it would have arrived in Chile in only 4.12 hr, that is, at 08:22 UT. In our case, the disturbance is observed starting from 11:30 UT, which means that if it was generated by the eruption, it should have traveled at the averaged horizontal speed of ∼340–350 m/s. This is faster than the Lamb waves that we observe in Chile, and it is difficult to explain. Finally, it could be a "regular" TID not related to the eruption but it's not typical for TID of these periods to have such velocities. Future modeling works will help to better understand the Tonga explosion mysteries, including this observation.

CVID#3 is observed at 18:00–21:00 UT, starting from ∼13.6 hr after the USGS onset time. The G32 hodochron (Figure 4e) shows the amplitude peaks for this CVID at about 1.7 TECU. The estimated velocities are in the range of 200 m/s, which is typical of tsunami gravity wave velocities. The waveforms (Figure 4f) and the spectral content (the peak ∼0.9 mHz, Figure S9 in Supporting Information S1), also confirm this pattern to represent the tsunami waves. Similar TEC signatures are observed by other satellites (G18 and G21 hodochrons in Figure S10 in Supporting Information S1).

We notice that the Lamb-induced CVID and the tsunami CVID both follow their respective simulated wavefronts in the near field, with the same trend direction. In the far-field, their propagation patterns differ, with the Lamb-induced CVID propagating along the Lamb waveform and the tsunami CVID following the Chilean coastline (Figure S5d in Supporting Information S1). This is due to the different paths each wave takes through the atmosphere and ocean, respectively.

Movie S2 also shows a time delay between the Lamb wave passage and its ionospheric signature in South America. To estimate this delay, we use the procedure aforementioned. We found the delay to be ∼15 min (Figure 3c, bottom panel), similar to our results in New Zealand-New Caledonia.

It should be emphasized that we only used a few TEC time series around the two case study zones to estimate the delay. Therefore, it might not be enough to provide the full picture of the coupling between the Lamb wave and the ionosphere. Further studies will be necessary to better understand the ionospheric propagation of Lamb waves.

Regarding the delay between the theoretical arrival of Lamb wave and the DART measurements observed in the near-field of the HTHH volcano, the Chilean DART data show only a small delay around couples of minutes (Figures 3c and 3d). This could be explained by a deep bathymetry of the Pacific Ocean around Chile, that affected the velocity of the air-sea wave (Yamada et al., 2022). Finally, it was not possible to perform the inversion for the eruption onset time and Lamb wave velocity because of close arrival times of the Lamb wave at the four DART stations and the 15 min sampling rate.

4. Conclusions

The extraordinary HTHH eruption affected the atmosphere and the oceans all over the world. We performed the first joint analysis of the eruption effects in oceanic and ionospheric data in New Caledonia-New Zealand and Chile-Argentina.

We recorded the effects of the Lamb wave and of the regular tsunami in both oceanic data and ionospheric observations. The Lamb wave passage did not create remarkable sea-surface fluctuations but was clearly identified in DART data and poorly recognized in tide gauges. In the ionosphere, Lamb wave-related disturbances had a great amplitude (peaking around 1.1 TECU for both areas). The regular tsunami caused major variations in sea-surface heights (∼1 m near the volcano and ∼2 m along the Chilean coastline), whereas the associated ionospheric perturbation was quite small, half the size of the Lamb wave perturbation.

Finally, for the first time, we estimated the time delay between the Lamb wave propagation and its signature in the ionosphere. The delay ranges between 12 and 20 min, that is, in-between the delay of acoustic and gravity waves.

Further analyses of this delay are of utmost importance for future hazard management strategies, as well as for a more accurate understanding of Lamb wave coupling with the ionosphere.

Data Availability Statement

GNSS data are available from the New Caledonia BANIAN network (www.banian.gouv.nc/Map/SensorMap.aspx) from the Chilean CSN (www.csn.uchile.cl/red-sismologica-nacional/red-gps/), and the Argentinian RAMSAC (Piñón et al., 2018). DART observations are from the NOAA data archives (www.ngdc.noaa.gov/mgg/global/ and www.ngdc.noaa.gov/hazard/dart/2022tonga.html). The coastal-sea-level measurements are publicly available via the Intergovernmental Oceanographic Commission of UNESCO (www.ioc-sealevelmonitoring.org/map.php).

Acknowledgments
This work was supported by the French Space Agency (CNES), projects "RealDetect" (EA and MR) and "UV-TECGEOX" (LR and EM), and by the French National Research Agency (ANR), projects ITEC (Grant ANR-19-CE04-0003, LR, EM, and DM) and IONO-DIET (Grant ANR-22-CE49-0011, EA and MR). LR and EM additionally acknowledge Université Côte d'Azur Investissement d'Avenir Idex. MR and EM were supported by the CNES PostDoctoral and PhD Fellowships. We thank P. Coïsson and F. Manta for fruitful discussions within an ad-hoc Geoazur-IPGP-NGI working group on the 2022 HTHH volcano eruption. The authors thank E. D'Anastasio for providing the GeoNet New Zealand 1-Hz-GNSS-data.

References

Aa, E., Zhang, S.-R., Erickson, P. J., Vierinen, J., Coster, A. J., Goncharenko, L. P., et al. (2022). Significant equatorial plasma bubbles and global ionospheric disturbances after the 2022 Tonga volcano eruption. *Authorea Preprints*. https://doi.org/10.1029/2022SW003101

Abercromby, R., Archibald, E., Bonney, T., Evans, F., Geikie, A., Judd, J., & others (1888). *The eruption of Krakatoa, and subsequent phenomena*. Report of the Krakatoa Committee of the Royal Society. Trübner & Company.

Amores, A., Monserrat, S., Marcos, M., Argüeso, D., Villalonga, J., Jordà, G., & Gomis, D. (2022). Numerical simulation of atmospheric lamb waves generated by the 2022 Hunga-Tonga volcanic eruption. *Geophysical Research Letters*, *49*(6), e2022GL098240. https://doi.org/10.1029/2022GL098240

Astafyeva, E. (2019). Ionospheric detection of natural hazards. *Reviews of Geophysics*, *57*(4), 1265–1288. https://doi.org/10.1029/2019RG000668

Astafyeva, E., Maletckii, B., Mikesell, T. D., Munaibari, E., Ravanelli, M., Coïsson, P., et al. (2022). The 15 January 2022 Hunga Tonga eruption history as inferred from ionospheric observations. *Geophysical Research Letters*, *49*(10), e2022GL098827. https://doi.org/10.1029/2022GL098827

Carvajal, M., Sepúlveda, I., Gubler, A., & Garreaud, R. (2022). Worldwide signature of the 2022 Tonga volcanic tsunami. *Geophysical Research Letters*, *49*(6), e2022GL098153. https://doi.org/10.1029/2022GL098153

Centro Sismológico Nacional, Universidad de Chile. (2022). Red sismológica nacional. Retrieved from http://www.csn.uchile.cl/red-sismologica-nacional/red-gps/

Dautermann, T., Calais, E., & Mattioli, G. S. (2009). Global positioning system detection and energy estimation of the ionospheric wave caused by the 13 July 2003 explosion of the Soufrière Hills Volcano, Montserrat. *Journal of Geophysical Research*, *114*(B2), B02202. https://doi.org/10.1029/2008JB005722

Digital Ionogram DataBase. (2022a). DIDBase fast station list. Retrieved from https://lgdc.uml.edu/common/DIDBDayStationStatistic?ursiCode=ND61R&year=2022&month=1&day=15

Digital Ionogram DataBase. (2022b). DIDBase fast station list. Retrieved from https://lgdc.uml.edu/common/DIDBDayStationStatistic?ursiCode=SMK29&year=2022&month=1&day=15

Direction des Infrastructures, de la Topographie et des Transports terrestres (DIIT). (2022). Banian. Retrieved from http://www.banian.gouv.nc/

Earthquake Commission, & GNS Science. (2022). Geological hazard information for New Zealand (GeoNet). Retrieved from https://www.geonet.org.nz/

Heki, K. (2006). Explosion energy of the 2004 eruption of the Asama Volcano, central Japan, inferred from ionospheric disturbances. *Geophysical Research Letters*, *33*(14), L14303. https://doi.org/10.1029/2006GL026249

Instituto Geográfico Nacional de la República Argentina. (2022). Red Argentina de Monitoreo satelital continuo (RAMSAC). Retrieved from https://www.ign.gob.ar/NuestrasActividades/Geodesia/Ramsac

Intergovernmental Oceanographic Commission of UNESCO. (2022). Sea level station monitoring facility. Retrieved from http://www.ioc-sealevelmonitoring.org/list.php

International Tsunami Information Center. (2022). 15 January 2022, Hunga-Tonga Hunga-Ha'apai volcanic eruption and tsunami. Retrieved from http://itic.ioc-unesco.org/index.php?option=com_content&view=article&id=2186&Itemid=3265

Kubota, T., Saito, T., & Nishida, K. (2022). Global fast-traveling tsunamis driven by atmospheric lamb waves on the 2022 Tonga eruption. *Science*, *377*(6601), eabo4364. https://doi.org/10.1126/science.abo4364

Kulichkov, S., Chunchuzov, I., Popov, O., Gorchakov, G., Mishenin, A., Perepelkin, V., et al. (2022). Acoustic-gravity lamb waves from the eruption of the Hunga-Tonga-Hunga-Hapai volcano, its energy release and impact on aerosol concentrations and tsunami. *Pure and Applied Geophysics*, *179*(5), 1–16. https://doi.org/10.1007/s00024-022-03046-4

Liu, C. H., Klostermeyer, J., Yeh, K. C., Jones, T. B., Robinson, T., Holt, O., et al. (1982). Global dynamic responses of the atmosphere to the eruption of Mount St. Helens on May 18, 1980. *Journal of Geophysical Research*, *87*(A8), 6281–6290. https://doi.org/10.1029/JA087iA08p06281

Liu, X., Xu, J., Yue, J., & Kogure, M. (2022). Strong gravity waves associated with Tonga volcano eruption revealed by saber observations. *Geophysical Research Letters*, *49*(10), e2022GL098339. https://doi.org/10.1029/2022GL098339

Lynett, P., McCann, M., Zhou, Z., Renteria, W., Borrero, J., Greer, D., et al. (2022). Diverse tsunamigenesis triggered by the Hunga Tonga-Hunga Ha'apai eruption. *Nature*, *609*(7928), 728–733. https://doi.org/10.1038/s41586-022-05170-6

Manta, F., Occhipinti, G., Hill, E. M., Perttu, A., Assink, J., & Taisne, B. (2021). Correlation between GNSS-TEC and eruption magnitude supports the use of ionospheric sensing to complement volcanic hazard assessment. *Journal of Geophysical Research: Solid Earth*, *126*(2), e2020JB020726. https://doi.org/10.1029/2020JB020726

Matoza, R. S., Fee, D., Assink, J. D., Iezzi, A. M., Green, D. N., Kim, K., et al. (2022). Atmospheric waves and global seismoacoustic observations of the January 2022 Hunga eruption, Tonga. *Science*, *377*(6601), 95–100. https://doi.org/10.1126/science.abo7063

Meng, X., Vergados, P., Komjathy, A., & Verkhoglyadova, O. (2019). Upper atmospheric responses to surface disturbances: An observational perspective. *Radio Science*, *54*(11), 1076–1098. https://doi.org/10.1029/2019RS006858

Munaibari, E., Rolland, L., Sladen, A., & Delouis, B. (2023). *Anatomy of the tsunami and Lamb waves-induced ionospheric signatures generated by the 2022 Hunga Tonga volcanic eruption (Version 1)*. Research Square. (Preprint).

Nishida, K., Kobayashi, N., & Fukao, Y. (2014). Background lamb waves in the Earth's atmosphere. *Geophysical Journal International*, *196*(1), 312–316. https://doi.org/10.1093/gji/ggt413

Nishikawa, Y., Yamamoto, M.-Y., Nakajima, K., Hamama, I., Saito, H., & Kakinami, Y. (2022). What excited tsunami from Tonga 2022 eruption? observation and theory. https://doi.org/10.21203/rs.3.rs-1513574/v1

NOAA. (2022a). Deep-ocean assessment and reporting of tsunamis (DART) description. Retrieved from https://nctr.pmel.noaa.gov/Dart/

NOAA. (2022b). January 15, 2022 Tonga tsunami. Retrieved from https://www.ngdc.noaa.gov/hazard/dart/2022tonga.html

Omira, R., Ramalho, R., Kim, J., González, P., Kadri, U., Miranda, J., et al. (2022). Global Tonga tsunami explained by a fast-moving atmospheric source. *Nature*, *1–2*(7928), 734–740. https://doi.org/10.1038/s41586-022-04926-4

Piñón, D. A., Gómez, D. D., Smalley, R., Cimbaro, S. R., Lauría, E. A., & Bevis, M. G. (2018). The history, state, and future of the Argentine continuous satellite monitoring network and its contributions to geodesy in Latin America. *Seismological Research Letters*, *89*(2A), 475–482. https://doi.org/10.1785/0220170162

Proudman, J. (1929). The effects on the sea of changes in atmospheric pressure. *Geophysical Supplements to the Monthly Notices of the Royal Astronomical Society*, *2*(4), 197–220. https://doi.org/10.1111/j.1365246X.1929.tb05408.x

Ravanelli, M., Crespi, M., & Foster, J. (2020). Tids detection from ship-based GNSS receiver: First test on 2010 maule tsunami. In *IGARSS 2020-2020 IEEE international geoscience and remote sensing symposium* (pp. 6846–6849). https://doi.org/10.1109/IGARSS39084.2020.9324549

Ravanelli, M., Occhipinti, G., Savastano, G., Komjathy, A., Shume, E. B., & Crespi, M. (2021). GNSS total variometric approach: First demonstration of a tool for real-time tsunami genesis estimation. *Scientific Reports*, *11*(1), 1–12. https://doi.org/10.1038/s41598-021-82532-6

Santellanes, S. R., Ruiz-Angulo, A., & Melgar, D. (2022). Tsunami waveform stacking and complex tsunami forcings from the Hunga-Tonga eruption. *Pure and Applied Geophysics*, 1–15. https://doi.org/10.1007/s00024-022-03200-y

Savastano, G., Komjathy, A., Verkhoglyadova, O., Mazzoni, A., Crespi, M., Wei, Y., & Mannucci, A. J. (2017). Real-time detection of tsunami ionospheric disturbances with a stand-alone GNSS receiver: A preliminary feasibility demonstration. *Scientific Reports*, *7*(1), 46607. https://doi.org/10.1038/srep46607

Shestakov, N., Orlyakovskiy, A., Perevalova, N., Titkov, N., Chebrov, D., Ohzono, M., & Takahashi, H. (2021). Investigation of ionospheric response to June 2009 sarychev peak volcano eruption. *Remote Sensing*, *13*(4), 638. https://doi.org/10.3390/rs13040638

Shults, K., Astafyeva, E., & Adourian, S. (2016). Ionospheric detection and localization of volcano eruptions on the example of the April 2015 Calbuco events. *Journal of Geophysical Research: Space Physics*, *121*(10), 10303–10315. https://doi.org/10.1002/2016JA023382

Symons, G. J., Judd, J. W., Strachey, R., Wharton, W. J. L., Evans, F. J., Russell, F. A. R., et al. (1888). *The eruption of Krakatoa: And subsequent phenomena*. Trübner & Company.

Themens, D. R., Watson, C., Žagar, N., Vasylkevych, S., Elvidge, S., McCaffrey, A., et al. (2022). Global propagation of ionospheric disturbances associated with the 2022 Tonga volcanic eruption. *Geophysical Research Letters*, *49*(7), e2022GL098158. https://doi.org/10.1029/2022GL098158

USGS. (2022). Earthquake hazard program. Retrieved from https://earthquake.usgs.gov/earthquakes/eventpage/us7000gc8r/executive

Vergoz, J., Hupe, P., Listowski, C., Le Pichon, A., Garc´es, M., Marchetti, E., et al. (2022). IMS observations of infrasound and acoustic-gravity waves produced by the January 2022 volcanic eruption of Hunga, Tonga: A global analysis. *Earth and Planetary Science Letters*, *591*, 117639. https://doi.org/10.1016/j.epsl.2022.117639

Vilibić, I., Šepić, J., Rabinovich, A. B., & Monserrat, S. (2016). Modern approaches in meteotsunami research and early warning. *Frontiers in Marine Science*, *3*, 57. https://doi.org/10.3389/fmars.2016.00057

Watada, S., & Kanamori, H. (2010). Acoustic resonant oscillations between the atmosphere and the solid Earth during the 1991 Mt. Pinatubo eruption. *Journal of Geophysical Research*, *115*(B12), B12319. https://doi.org/10.1029/2010JB007747

Watanabe, S., Hamilton, K., Sakazaki, T., & Nakano, M. (2022). First detection of the Pekeris internal global atmospheric resonance: Evidence from the 2022 Tonga eruption and from global reanalysis data. *Journal of the Atmospheric Sciences*, *79*(11), 3027–3043. https://doi.org/10.1175/jas-d-22-0078.1

Wright, C., Hindley, N., Alexander, M. J., Barlow, M., Hoffmann, L., Mitchell, C., et al. (2022). Tonga eruption triggered waves propagating globally from surface to edge of space. *Earth and Space Science Open Archive*. https://doi.org/10.1002/essoar.10510674.1

Yamada, M., Ho, T. C., Mori, J., Nishikawa, Y., & Yamamoto, M. Y. (2022). Tsunami triggered by the lamb wave from the 2022 Tonga volcanic eruption and transition in the offshore Japan region. *Geophysical Research Letters*, *49*(15). e2022GL098752. https://doi.org/10.1029/2022GL098752

References From the Supporting Information

Amante, C., & Eakins, B. W. (2009). *ETOPO1 1 arc-minute global relief model: Procedures, data sources and analysis*. National Geophysical Data Center. https://doi.org/10.7289/V5C8276M

Aster, R. C., Brian Borchers, & Thurber, C. H. (2018). *Parameter estimation and inverse problems*. Elsevier.

Wessel, P. (2009). Analysis of observed and predicted tsunami travel times for the Pacific and Indian Oceans. *Pure and Applied Geophysics*, *166*(1), 301–324. https://doi.org/10.1007/s00024-008-0437-2